Simplified Operation and Control of a Series-Resonant Balancing Converter for Bipolar DC Grids

Yadav, Sachin; Bauer, Pavol; Qin, Zian

DOI
10.1109/JESTPE.2024.3397830

Publication date
2024

Document Version
Final published version

Published in
IEEE Journal of Emerging and Selected Topics in Power Electronics

Simplified Operation and Control of a Series-Resonant Balancing Converter for Bipolar DC Grids

Sachin Yadav, *Graduate Student Member, IEEE*, Pavol Bauer, *Senior Member, IEEE*, and Zian Qin, *Senior Member, IEEE*

***Abstract*— Balancing converters play a pivotal role in bipolar dc grids, and while numerous topologies have been explored, many suffer from drawbacks, such as reliance on bulky passive components, limited soft-switching capabilities, or complex control mechanisms. This article introduces an LC series-resonant balancing converter topology that addresses these issues, featuring smaller passive components, the ability to achieve soft switching across its entire operational range, and simplified control with proper design. By operating in the capacitive region, the converter ensures soft switching for the complete load range, enabling all switches to achieve zero voltage switching (ZVS) turn on. The study reveals that the converter's power flow depends on both the switching frequency (f_{sw}) and the phase shift angle (ϕ), but notably, when the resonant inductor value is kept sufficiently low, f_{sw} and ϕ become decoupled, simplifying power flow control. In addition, this article provides detailed design guidelines for the converter's resonant tank and validates the operation and control of the converter through an experimental setup.**

***Index Terms*— DC–DC converter, dc grid, modulation, resonant power converters, soft switching, zero voltage switching (ZVS).**

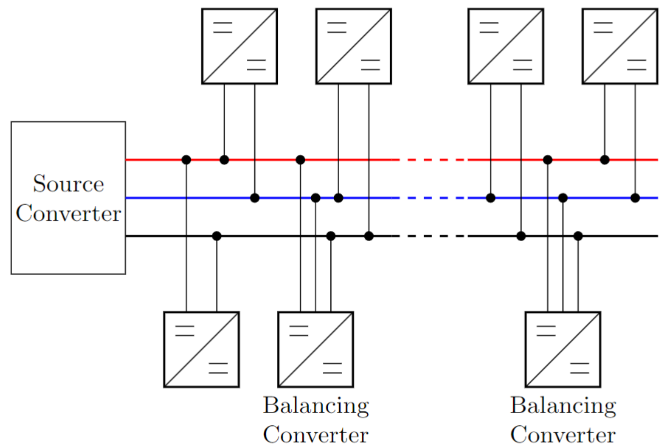

Fig. 1. Representation of a bipolar dc grid showing the installation of various load and balancing converters connections.

I. Introduction

Bipolar dc grids halve the voltage potential between the poles and the ground, compared with unipolar dc grids. The requirement of the insulator, as well as the circuit breakers, is, thus, reduced. In The Netherlands, bipolar dc grids have been installed in office buildings and greenhouses [1], [2]. Furthermore, bipolar dc grids are also finding applications in large ships for improving survivability and supplying the hotel loads [3], [4]. If the two poles are well balanced, there will be much less load in the neutral line, and therefore, the neutral line can be much smaller than the two poles. So, the cable costs of the bipolar dc grid are not necessarily considerably higher than a unipolar dc grid with the same voltage (between the two poles) and power rating. Furthermore, it is not necessary to have three cables for the whole grid. Three conductors can be installed only in the region where a pole-to-neutral connection is needed [5]. Nonetheless, the load of the two poles could be unbalanced, especially in applications where the number of loads is small; then, a power load plug-in or plug-out on one pole can quickly create an imbalance. On the other hand, in a large grid with multiple grounding points, the unbalance at the neutral can also lead to circulating currents through the neutral points [6], [7]. Balancing circuits are, therefore, necessary auxiliary devices to enhance the robustness of the bipolar dc grids.

Power balancing in bipolar dc grids can be done in two ways. One of the ways is to use the main converter to balance the power flowing into the two poles [8], [9], [10]. However, these techniques are feasible only when the power distribution network is small. This is because if the unbalance happens at the end of a long distribution line, the neutral current through the converter will have to cover a long distance, which can incur high losses in the system. Furthermore, a neutral is always required to transfer power to the unbalanced load, increasing the system costs [5]. The second way of balancing the bipolar dc grid is using several smaller power capacity converters, as illustrated in Fig. 1. Several balancing circuits have been discussed in the literature, including inverting-type topologies, such as bidirectional buck–boost converters,

Manuscript received 12 September 2023; revised 21 March 2024; accepted 29 April 2024. Date of publication 6 May 2024; date of current version 2 August 2024. This work was supported by Nederlandse Organisatie voor Wetenschappelijk Onderzoek (NWO) under Grant 17628. Recommended for publication by Associate Editor Jeehoon Jung. *(Corresponding author: Zian Qin.)*

The authors are with the DC Systems Energy Conversion and Storage, Electrical Sustainable Energy, Faculty of EEMCS, Delft University of Technology, 2628 CD Delft, The Netherlands (e-mail: S.Yadav-1@tudelft.nl; Z.Qin-2@tudelft.nl).

Color versions of one or more figures in this article are available at https://doi.org/10.1109/JESTPE.2024.3397830.

Digital Object Identifier 10.1109/JESTPE.2024.3397830

Cuk converters, SEPIC converters, and more [8], [11], [12], [13], [14], [15], [16]. Resonant balancing circuits, which can achieve high power density due to relatively small passive components, can rarely be found in the literature. Sano and Fujita [17] and [18] have used a similar topology for capacitor balancing in multilevel converters. The authors refer to the converter as a resonant-switched capacitor converter and use the converter in the inductive region of the resonant tank. Similarly, Hang et al. [19] use the same converter to balance dc link capacitor voltage in a five-level flying multilevel converter for wind turbine applications. A recent article also uses the same topology for balancing the grid, which works in the inductive region [20]. The operating principle of the balancing converter in [19] and [20] is similar to that in [17]. All the above converters are operated in the inductive region (f_{sw} is higher than the resonant frequency of the LC resonant tank). However, in the inductive region, the converter cannot have zero voltage switching (ZVS) turn on of the switches in the whole operating range [21]. In this article, a resonant converter operating in the capacitive region (f_{sw} is lower than resonant frequency) is attempted to balance a bipolar dc grid. It is found that the converter can show the ZVS turn on for all the switches in the whole operating range. ZVS capability is vital, as it reduces the common-mode EMI emissions [22].

With operation near resonant frequency, the power from one pole to another is dominated by the voltage difference between the poles. The balancing becomes ineffective when the voltage difference is negligible, even if the load of the two poles is still significantly uneven. A power control approach of the resonant balancing circuit is proposed to solve the issue of the voltage difference. First, a variable f_{sw} is applied to effectively control the power flow between the poles. The side effect is that the circulating current scales as f_{sw} deviates from the resonant frequency. Then, a variable ϕ is utilized with the variable f_{sw} to minimize the circulating current and maintain the switches' ZVS turn on. The analysis also found that with a small value of the characteristic impedance of the resonant tank, the relationship between f_{sw} and ϕ can be decoupled, thus making the control more straightforward.

The application of this topology for bipolar dc grid balancing by the same authors was provided in [23]. This article expands the previous literature with the following additions as the main contributions.

1) f_{sw} and ϕ conditions for ZVS turn on in all the switches for all operating modes are provided.
2) A control scheme is proposed with decoupled relationship between f_{sw} and ϕ, which makes the voltage balancing control simple.
3) Design guidelines for selecting resonant tank elements are provided to enable the converter's more straightforward power flow control.

The rest of this article is structured as follows. The fundamental operation principle and the proposed power control are introduced in Section II. The guidelines for designing a series-resonant balancing converter are discussed in Section III. The control scheme for power flow control of the converter is discussed in Section IV. The experimental results for the converter are shown and discussed in Section V. Finally, Section VI concludes this article.

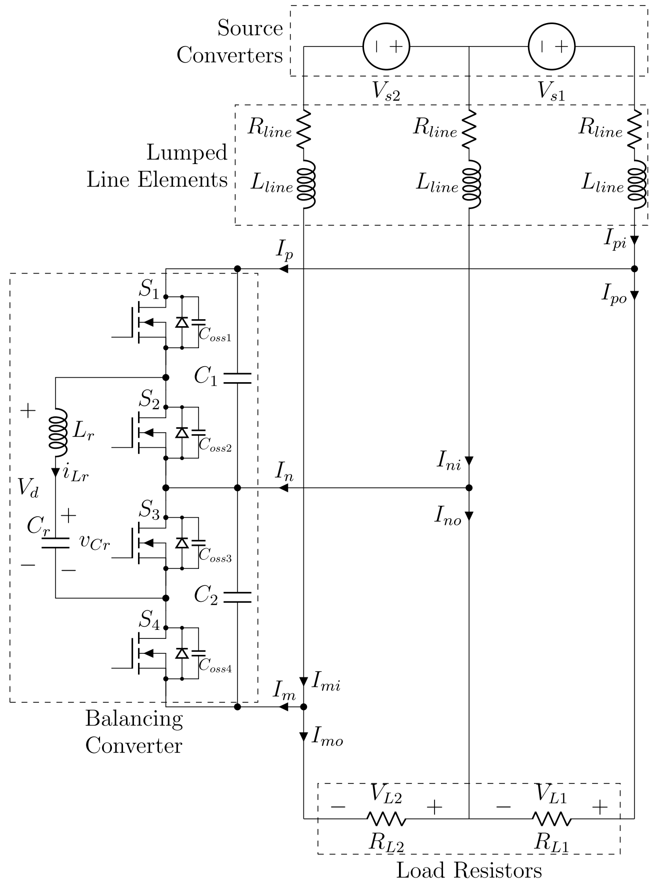

Fig. 2. Schematic of a bipolar dc grid with the integration of balancing converter.

II. Operating Principle and Power Flow Control

The schematic of the resonant balancing circuit, along with an example bipolar dc grid, is shown in Fig. 2. The converter consists of four switches S_1–S_4, a resonant inductor (L_r), a resonant capacitor (C_r), and two dc-link capacitors C_1 and C_2. I_{xi} ($x \in \{p, n, m\}$) represents the grid side currents, I_{xo} represents the load side currents, and I_x represents the current flowing into the balancing converter terminals. During steady-state operation, the average current through the converter is shown in Fig. 3. Two scenarios for grid imbalance are possible. In the first scenario shown in Fig. 3(a), a higher load is connected between the + and neutral poles. In the second scenario shown in Fig. 3(b), a higher load is connected between the neutral and − poles. When the grid is balanced, the same amount of current, represented by ($I_{\mathrm{bal}}/2$), flows through the + and − conductors of the balancing converter. The sum of these currents, I_{bal}, flows through the neutral conductor of the balancing converter.

Ideally, the converter can operate at the resonant frequency to balance the voltage of two poles (+ and −) to the neutral. However, depending on the impedance of the voltage sources and the cables, while the voltage difference between the two poles is still negligible, the load of the two poles can be significantly unbalanced. In this case, the balancing circuit with the ideal resonant operation cannot shift a proper amount of load power from one pole to another. A power control approach with variable f_{sw} and ϕ is

TABLE I
SWITCHING PATTERNS IN THE PROPOSED CONTROL

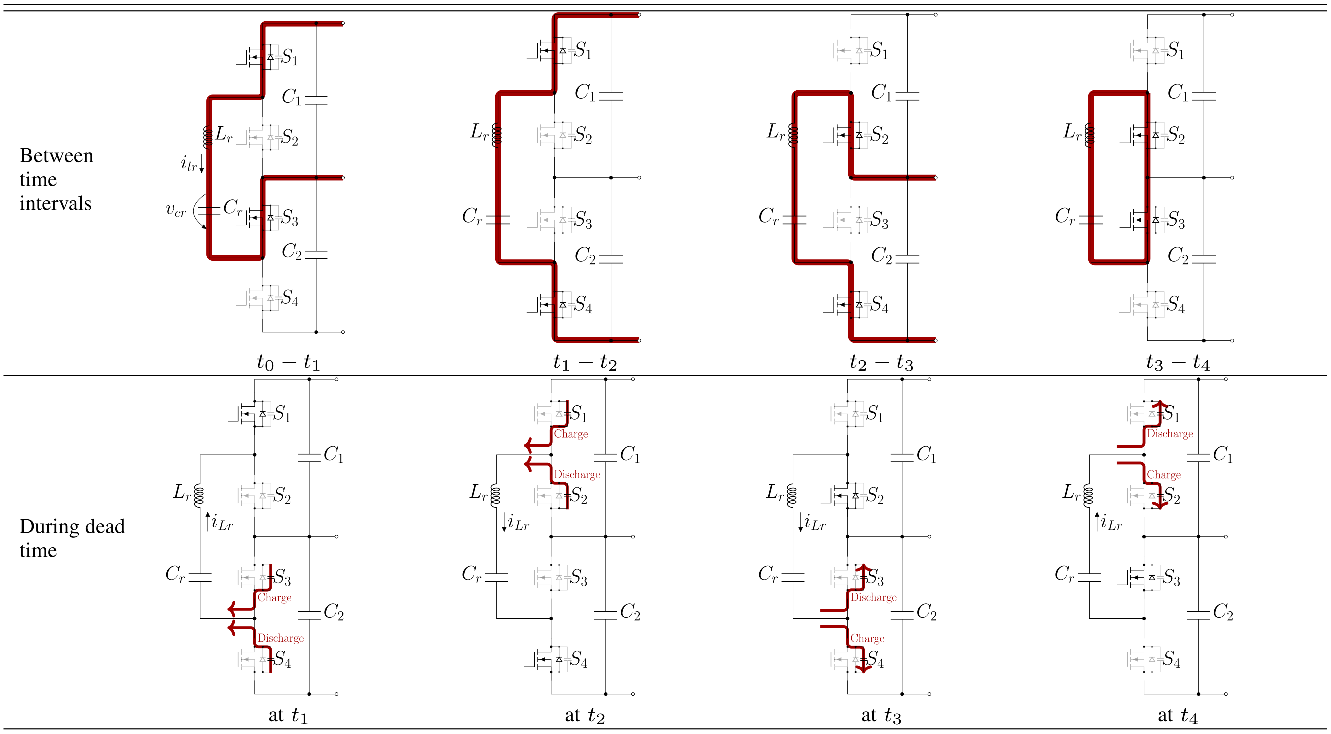

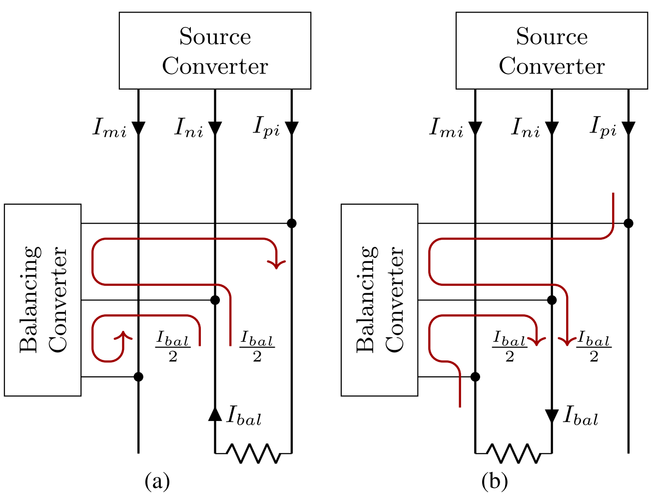

Fig. 3. Flow of the balancing current when the converter completely balances the grid. (a) Flow of the balancing current when there is a higher load between + and n. (b) Flow of the balancing current when there is a higher load between n and −.

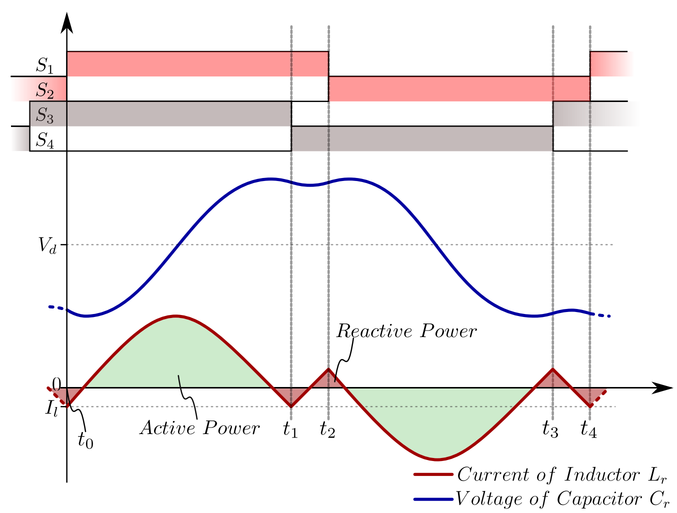

Fig. 4. Elaboration of switching patterns and resonant tank states with the proposed control.

proposed to solve this issue, and more details are elaborated below.

A. Switching Pattern Analysis

The proposed power control comprises the switching pattern, as shown in Fig. 4 and Table I. The converter operation is also elaborated below.

1) *t_0–t_1:* During this interval, S_1 and S_3 are conducting. C_r is charging, and L_r limits the current rate of change. At the end of this interval, S_3 is turned off. The current through L_r (i_{Lr}) flows in the opposite direction, as seen in Fig. 4. During the dead time between S_3 and S_4, this current discharges and charges the switch output capacitance (C_{oss}) of S_4 and S_3, respectively. Thus, S_4 exhibits ZVS turn on.
2) *t_1–t_2:* This is the duration of ϕ. S_3 is turned off during this interval, and S_1 and S_4 conduct current. Hence, there is a higher voltage present across the resonant tank. Due to this stage, the charge is pumped into C_r. This extra charge stored in C_r boosts the voltage of C_r. S_4 is turned on with ZVS. ϕ is set, such that the L_r current

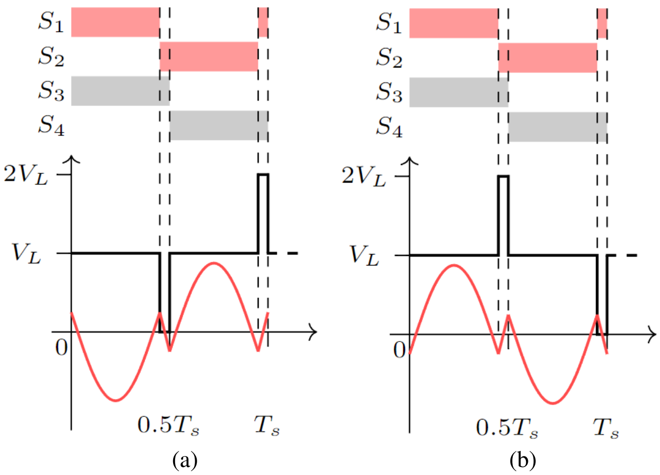

Fig. 5. Resonant tank voltages along with the resulting L_r current. (a) Lagging ϕ. (b) Leading ϕ.

changes direction by the end of this interval. At the end of this interval, S_1 is turned off, and the positive L_r current discharges and charges the C_{oss} of S_2 and S_1, respectively. Thus, S_2 exhibits ZVS turn on.

3) t_2–t_3: During this interval, S_1 is off, and S_2 is turned on. The resonant tank is connected to the neutral and negative poles through switches S_2 and S_4. The L_r current reverses direction, and C_r is discharged as the energy is transferred to the load. At the end of this interval, the L_r current becomes positive, as seen in Fig. 4. The positive current discharges and charges the C_{oss} of S_3 and S_4, respectively. Thus, S_3 exhibits ZVS turn on.
4) t_3–t_4: This is the duration of ϕ. S_4 is turned off during this interval, and S_3 is turned on. Similar to interval $\mathbf{t_1}$–$\mathbf{t_2}$, the L_r current becomes negative at the end of this interval. The L_r current discharges and charges the C_{oss} of S_1 and S_2, respectively. Thus, S_1 exhibits ZVS turn on.

The converter operates with a phase shift angle (ϕ) between the upper and lower half-bridges. Furthermore, the converter operates in the capacitive region of the resonant tank. This means that f_{sw} is below the resonant frequency of the resonant tank. The resonant frequency is given by

$$f_r = \frac{1}{2\pi\sqrt{L_r C_r}}. \tag{1}$$

With the lagging and leading ϕ between the upper and lower half-bridges, the voltage profile across the resonant tank is shown in Fig. 5(a) and (b), respectively. The voltage V_L is defined by (2). When the voltage across the resonant tank suddenly drops to zero, there is also a voltage drop across L_r. During this duration, C_r and L_r are shorted through switches S_2 and S_3. Hence, the current through L_r is suddenly decreased. This process is illustrated in Fig. 5(a). When the resonant tank voltage is $2V_L$, there is suddenly a high voltage across L_r. Therefore, the current rises rapidly. This change in voltage across L_r is illustrated in Fig. 5(b).

From the discussion above, it is clear that if the ϕ is reversed, the average current direction through the converter can be reversed. Hence, the power flow direction can be controlled.

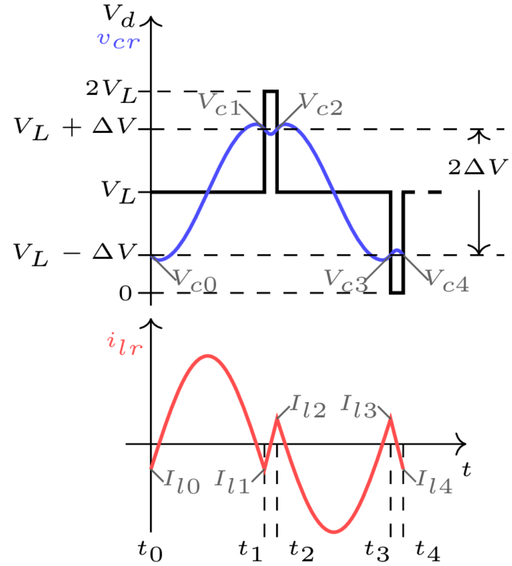

Fig. 6. Time stamps for L_r current and C_r voltage with a leading ϕ.

B. Switching Frequency Calculation

In Section II-A, the qualitative analysis showed the soft-switching capabilities of the balancing converter. To ensure ZVS turn on of all the switches under any operating condition, it is necessary to correctly calculate f_{sw} and ϕ between the upper and lower half-bridges. This section gives the calculations for f_{sw} and ϕ. The assumptions for the calculations are as follows.

1) Under steady-state conditions, the converter operates with balanced voltages between the +n and n− poles. The implication of this assumption is given in the following equation:

$$V_{L1} = V_{L2} = V_L. \tag{2}$$

2) The L_r current magnitude at each switching instance is the same. However, the direction of the current can be different depending on the switching instance. The L_r current magnitude is denoted by I_{l0}.

The L_r current and C_r voltage are shown in Fig. 6. The converter behaves as a typical resonant converter with piecewise behavior in the four distinct regions the phase shifting creates. The equations for L_r current and C_r voltage for the series LC circuit are given in the following equation:

$$i_{\text{lr}}(t) = \begin{cases} I_{l0}\cos(\omega_0 t) + \dfrac{V_d - V_{c0}}{Z_0}\sin(\omega_0 t), & t_0 \le t < t_1 \\ I_{l1}\cos(\omega_0 t) + \dfrac{V_d - V_{c1}}{Z_0}\sin(\omega_0 t), & t_1 \le t < t_2 \\ I_{l2}\cos(\omega_0 t) + \dfrac{V_d - V_{c2}}{Z_0}\sin(\omega_0 t), & t_2 \le t < t_3 \\ I_{l3}\cos(\omega_0 t) + \dfrac{V_d - V_{c3}}{Z_0}\sin(\omega_0 t), & t_3 \le t < t_4 \end{cases} \tag{3}$$

$$v_{\mathrm{cr}}(t)=\begin{cases}V_d-(V_d-V_{c0})\cos(\omega_0 t)\\ \qquad +I_{l0}Z_0\sin(\omega_0 t), & t_0\le t<t_1\\ V_d-(V_d-V_{c1})\cos(\omega_0 t)\\ \qquad +I_{l1}Z_0\sin(\omega_0 t), & t_1\le t<t_2\\ V_d-(V_d-V_{c2})\cos(\omega_0 t)\\ \qquad +I_{l2}Z_0\sin(\omega_0 t), & t_2\le t<t_3\\ V_d-(V_d-V_{c3})\cos(\omega_0 t)\\ \qquad +I_{l3}Z_0\sin(\omega_0 t), & t_3\le t<t_4\end{cases} \quad (4)$$

where V_d is the voltage across the LC resonant tank, I_{l0} is the initial L_r current, ω_0 is the natural angular frequency of the resonant tank, Z_0 is the characteristic impedance, and V_{c0} is the initial voltage across C_r. Furthermore, for the case in Fig. 6, V_d also varies with time as given by the following equation:

$$V_d=\begin{cases}V_L, & t_0\le t<t_1\\ 2V_L, & t_1\le t<t_2\\ V_L, & t_2\le t<t_3\\ 0, & t_3\le t<t_4.\end{cases} \quad (5)$$

The L_r current waveform can be broken down into smaller time intervals, as shown in Fig. 6. As explained in Section II-A, the whole L_r current can be subdivided into four intervals from t_0 to t_4. The currents at these five instances, namely, t_0, t_1, t_2, t_3, and t_4, are denoted by I_{l0}, I_{l1}, I_{l2}, I_{l3}, and I_{l4}, respectively, as shown in Fig. 6. The formulas to determine f_{sw} and ϕ are given below, assuming that the magnitude of all the initial L_r currents can be made equal, such that

$$I_{l0}=I_{l1}=-I_{l2}=-I_{l3}=I_{l4} \quad (6)$$

$$I_{\mathrm{coss}}=V_L\sqrt{\frac{8C_{\mathrm{oss}}}{3L_r}}. \quad (7)$$

The magnitude of I_{l0} is selected to be higher than the value of I_{coss} given in (7) to ensure the ZVS turn on of the switches. The time intervals can be calculated using (3) and (4). At t_0, S_1 is turned on when the L_r current is I_{l0}. Due to the resonant operation, the current rises and then drops. S_3 should be turned off when the L_r current again becomes equal to I_{l0}. Using these assumptions, we solve (3) and get

$$t_1-t_0=\frac{2}{\omega_0}\left[\frac{\pi}{2}-\mathrm{atan}\left(\frac{Z_0 I_{l0}}{V_L-V_{c0}}\right)\right] \quad (8)$$

and

$$t_2-t_1=\frac{2}{\omega_0}\left[\frac{\pi}{2}-\mathrm{atan}\left(-\frac{2V_L-V_{c1}}{Z_0 I_{l0}}\right)\right]. \quad (9)$$

Interestingly, the values of V_{c0} and V_{c1} are related to each other

$$\begin{aligned}V_{c0}&=V_L-\Delta V\\ V_{c1}&=V_L+\Delta V.\end{aligned} \quad (10)$$

As it is assumed that the resonant tank states are symmetric, the duration (t_1-t_0) is equal to (t_3-t_2), and (t_2-t_1) is equal to (t_4-t_3). Hence, f_{sw} can be calculated as follows:

$$f_{\mathrm{sw}}=\frac{1}{2((t_2-t_1)+(t_1-t_0))}=\frac{1}{2(t_2-t_0)}. \quad (11)$$

C. Power Flow Calculations

Only the variable ΔV is unknown in the equations above. Hence, using (8)–(11), a relationship can be found out to finally eliminate ΔV. The relationship is given by

$$\frac{Z_0^2 I_{l0}^2-\Delta V(V_L-\Delta V)}{Z_0(I_{l0}(V_L-\Delta V)+I_{l0}\Delta V)}=\tan\left(\pi-\frac{\omega_0}{4f_{\mathrm{sw}}}\right). \quad (12)$$

Solving (12) for ΔV, we get

$$\Delta V=\frac{V_L}{2}-\sqrt{\left(\frac{V_L}{2}\right)^2-I_{l0}^2Z_0^2-\tan\left(\frac{\omega_0}{4f_{\mathrm{sw}}}\right)I_{l0}V_LZ_0}. \quad (13)$$

The output current delivered by the converter is the rectified current in the resonant tank in one cycle. The output current can be found using the voltage change in C_r, as the active power flowing through C_r will dictate the voltage change in C_r. Hence, the output current is found using

$$I_o=4\ f_{\mathrm{sw}}C_r\Delta V. \quad (14)$$

Assuming that the voltages at the two poles are balanced at steady state, the power flowing through the balancing converter is found using

$$\begin{aligned}P_o&=4\ f_{\mathrm{sw}}C_rV_LI_o\\ &=4\ f_{\mathrm{sw}}C_rV_L\\ &\quad\times\left[\frac{V_L}{2}-\sqrt{\left(\frac{V_L}{2}\right)^2-I_{l0}^2Z_0^2-\tan\left(\frac{\omega_0}{4f_{\mathrm{sw}}}\right)I_{l0}V_LZ_0}\right].\end{aligned} \quad (15)$$

ϕ as a function of f_{sw} and I_{l0} needed to achieve the change in current during these intervals is given by the following equation:

$$\begin{aligned}&\phi(f_{\mathrm{sw}},I_{l0})\\ &\quad=\frac{2\pi f_{\mathrm{sw}}}{\omega_0}\\ &\qquad\times\left[\pi+2\tan^{-1}\left(\frac{V_L}{2I_{l0}Z_0}\right.\right.\\ &\qquad\left.\left.+\sqrt{\left(\frac{V_L}{2I_{l0}Z_0}\right)^2-\frac{Z_0}{I_{l0}V_L}\tan\left(\frac{\omega_0}{4f_{\mathrm{sw}}}\right)-1}\right)\right].\end{aligned} \quad (16)$$

Equations (15) and (16) can create a power flow map. A power flow map is shown in Fig. 7 for the converter parameters given in Section V.

III. Converter Design

This section discusses the various aspects of choosing the value of L_r and C_r. Also, a comparison of the converter with other balancing converter topologies is given.

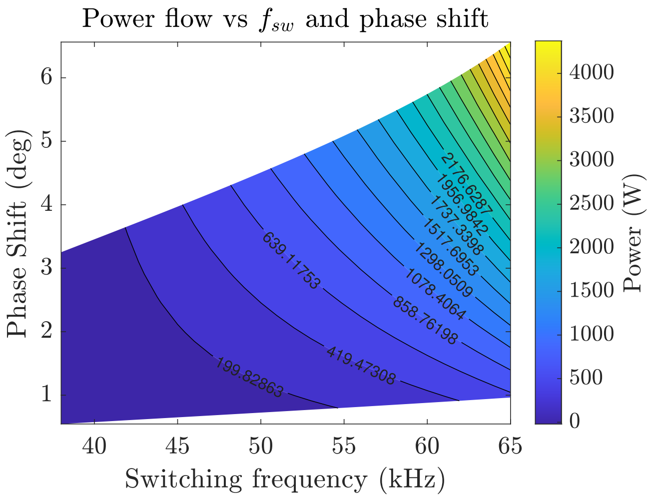

Fig. 7. Figure showing the power flow with respect to f_{sw} and ϕ.

A. Choice of L_r

Using (16), the phase shift time duration (t_ϕ) for different values of f_{sw} and I_{l0} can be deduced as follows:

$$t_\phi(f_{\text{sw}}, I_{l0}) = \frac{\phi(f_{\text{sw}}, I_{l0})}{2\pi f_{\text{sw}}} = \frac{1}{\omega_0}\left[\pi + 2\tan^{-1}\left(\frac{V_L}{2I_{l0}Z_0} + \sqrt{\left(\frac{V_L}{2I_{l0}Z_0}\right)^2 - \frac{Z_0}{I_{l0}V_L}\tan\left(\frac{\omega_0}{4f_{\text{sw}}}\right) - 1}\right)\right]. \quad (17)$$

In (17), with fixed V_L, I_{l0}, and Z_0, there is only the term $\tan(\omega_0/4f_{\text{sw}})$, which changes with f_{sw}. However, this term does not change considerably compared with the other terms under the square root. With this assumption, (17) can be simplified as follows:

$$t_\phi(I_{l0}) \approx \frac{1}{\omega_0}\left[\pi + 2\tan^{-1}\left(\frac{V_L}{I_{l0}Z_0}\right)\right]. \quad (18)$$

It can be observed that (18) has no dependence upon f_{sw}. Thus, for a particular I_{l0}, a constant value of t_ϕ can be used. This finding dramatically simplifies the power flow control of the balancing converter. As discussed, I_{l0} is set above the minimum current required to achieve ZVS turn on in the MOSFETs as defined by (7).

B. Choice of C_r

During regular operation, the C_r consists of a dc bias and a voltage ripple. Furthermore, the whole L_r current passes through C_r. Due to this, the capacitors need to be thermally stable even with high-current conditions. For resonant converter applications, C0G dielectric capacitors are considered suitable [24]. This is because of their high purity and low tolerances [24], [25], [26]. The capacitance also does not change with temperature. Furthermore, the electric series resistance (ESR) is also relatively low.

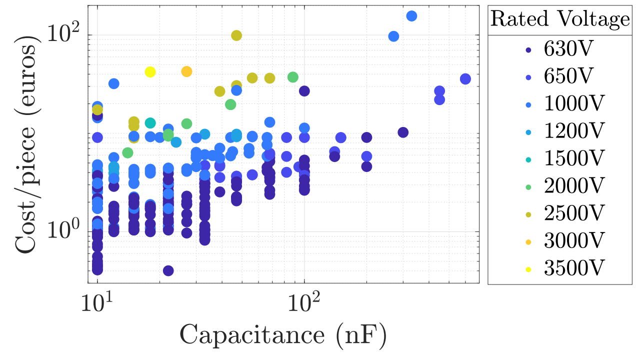

Fig. 8. Cost of C0G capacitors. Source: Digikey.com.

The C0G dielectric capacitors do have a few disadvantages. First, the dielectric constant of C0G is relatively low [24], [25], [26]. This means that the capacitance value of C0G compared with those of other ceramic capacitors (e.g., X7R) for the same size and voltage rating is much lower [27]. Due to this, the power density of the converter becomes lower. Second, ceramic capacitors' voltage and current ratings are limited and change with the frequency of operation [28]. Under normal conditions, the current rating increases with frequency. The voltage rating remains constant up to some frequency but reduces after this frequency. These ratings limit the operating range of the converter and, hence, are a constraint to the converter operation. Third, the cost of C0G capacitors is very high. Fig. 8 shows the cost of the C0G capacitors for different voltage ratings. The data were acquired from www.digikey.com. It can be seen that the price of high voltage and high capacitance can be as high as 160€/piece. Therefore, the choice of capacitance value significantly impacts converter costs for this application.

C. Comparison With Other Topologies

The topology used in this article is yet to be considered for the bipolar dc grid balancing application, as per the recent literature review [29]. The other converters in previous literature can also show ZVS turn on, which comes at the cost of larger passive components. To achieve ZVS turn on in all the switches, triangular current mode (TCM) is used [30]. During steady state, the current through the inductors for different topologies utilizing TCM is triangular, as shown in Table II. The ripple current through the inductor for the buck–boost converter can be calculated by

$$I_{l,\text{rip}} = 2(I_o + I_{\text{coss}}) \quad (19)$$

where I_o is the output load current and I_{coss} is the minimum current required to discharge the output capacitance of the semiconductor switches. In the interleaved buck–boost and Cuk converter, there are two inductors. The output current is supplied equally by the two separate inductors. Hence, the ripple current for the inductors in these topologies is given by

$$I_{l,\text{rip}} = I_o + 2I_{\text{coss}} \quad (20)$$

which is also shown in Table II. The required inductance value depends upon the applied voltage V_L, ripple current in (19),

TABLE II
COMPARISON OF VARIOUS BALANCING SOLUTIONS

Converter Topology	Buck-Boost	Interleaved Buck-Boost	Cuk	Series-Resonant (This work)
	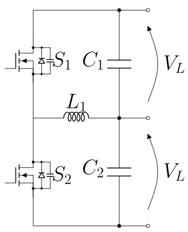	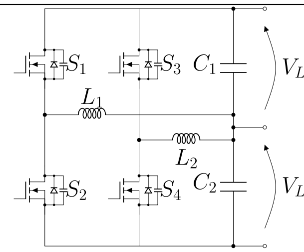	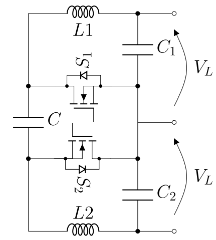	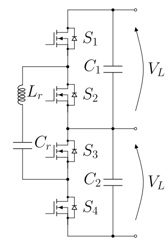
Inductor current waveforms	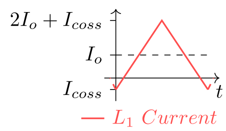	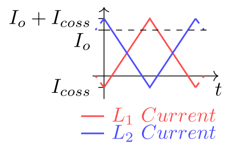	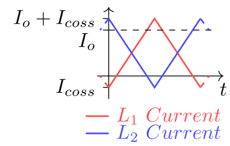	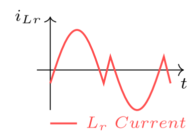
No. of Switches	2	4	2	4
Voltage Rating	$2V_L$	$2V_L$	$2V_L$	V_L
No. of Passives	1	2	3	2
Inductor Sizing	2.55	1.75	1.75	0.16
Switch loss distribution	Unequal	Unequal	Unequal	Equal
No. of control parameters	2	2	2	1

and minimum f_{sw} $f_{sw,min}$, as given in the following equation:

$$L_{req} = \frac{V_L}{I_{l,rip} f_{sw,min}}. \tag{21}$$

Various converters can be compared for the sizing of the inductor using the K_g method given in [31]. The value of K_g is given by

$$K_g = \frac{\rho L_{req}^2 I_{max}^2 10^8}{B_{max}^2 R K_u} \tag{22}$$

where B_{max} is the maximum allowed magnetic flux density of the core (assumed to be 300 mT for ferrite material), R is the total resistance of the conductor, and K_u is the utilization factor (assumed to be 0.4). A comparison of the resonant converter with other balancing solutions is shown in Table II. The comparison is made for a minimum f_{sw} of 30 kHz with ZVS turn-on capability for all the switches. The minimum current required for ZVS turn on (I_{coss}) is the same for all the switches, with a value of 6.7 A. The value of I_{coss} is chosen for the SiC power module used in the prototype for this work. The voltage V_L is considered to be 350VDC, and the rated power is 2 kW. Using (22), an indication of inductor size for the various topologies is given in Table II. For the inductor size calculations, an inductance of 180 μH is chosen for all the converters except the series-resonant converter. Because of the resonant nature, the inductance requirement for the series-resonant converter is very low at 7 μH. The value of I_{max} was chosen according to the maximum current at a power flow of 2 kW. It can be seen that the buck–boost converter has the largest inductor size, but only a single inductor is required. On the other hand, the inductor sizes of the Cuk and interleaved buck–boost converter are similar, but they require two inductors. On top of that, a Cuk converter requires an additional capacitor as a passive component. The resonant converter's inductor size is very low. This is because of the very small inductance requirement for this type of converter. The passive component sizing guidelines for the series-resonant balancing converter were discussed in Section III.

In examining the switch loss distribution among three topologies compared with the series-resonant topology, it is observed that the power flow direction results in one switch conducting at a significantly higher current than its counterpart, leading to an imbalance in switch losses despite the elimination of turn-on losses across all topologies [31]. This discrepancy introduces substantial turn-off losses in one switch over the other, necessitating a meticulously designed heat dissipation system to manage the unequal loss distribution effectively. Contrary to this, the series-resonant topology maintains a consistent current level across all switches throughout the entire load power range, ensuring uniform power loss across switches at any given moment. This characteristic significantly simplifies the thermal management requirements and enhances the overall efficiency and reliability of the system.

In the context of ideal buck–boost derived topologies, the theoretical model suggests that power flow is solely dependent on the switching frequency. However, practical applications reveal a nuanced complexity: achieving voltage balance and ensuring ZVS turn on for the switches necessitate a slight adjustment in the duty cycle in relation to the inductor current flow [32], [33]. Consequently, to attain the desired power flow and voltage equilibrium in these topologies, both the switching frequency and the duty cycle must be fine-tuned. This requirement starkly contrasts with the operation of the series-resonant converter, where, as delineated in Section III-A, an optimized design of the resonant inductor (L_r) allows for the control of power flow and voltage solely through adjustments in the switching frequency (f_{sw}), while maintaining a constant phase shift duration (t_ϕ). This simplification not only streamlines the control strategy but also enhances the efficiency

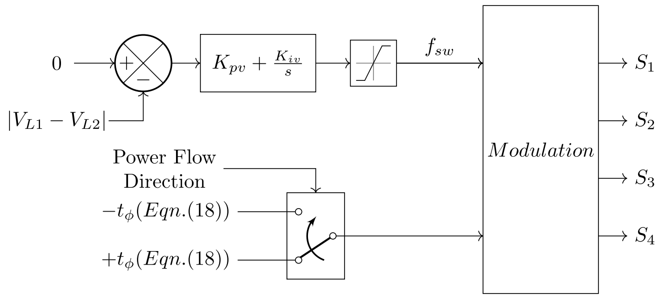

Fig. 9. Control flowchart for the converter.

and reliability of the series-resonant converter in practical implementations.

IV. Control Scheme

The simple control scheme presented in Fig. 9 operates the balancing converter in the closed loop. The control scheme entails changing both f_{sw} and ϕ using (15) and (16), respectively. As discussed above, with a sufficiently low L_r value, the t_ϕ can be kept constant. Hence, t_ϕ is calculated beforehand for a specific converter using (18). The positive or negative value of the duration refers to the leading or lagging t_ϕ, respectively. $+t_\phi$ means that the lower half-bridge (S_3 and S_4) is lagging the upper half-bridge (S_1 and S_2); $-t_\phi$ means that the lower half-bridge (S_3 and S_4) is leading the upper half-bridge (S_1 and S_2). The phase shift can be set as leading or lagging depending upon the power flow direction requirement. Determining power flow direction is out of the scope of this article, as it depends significantly on the grid parameters.

f_{sw} depends on the amount of power flow required between the $+$ and $-$ poles. Voltages V_{L1} and V_{L2} are sensed, and the absolute difference is compared with 0 to generate the voltage error. The error is fed through a PI controller to generate the setpoint for f_{sw}. K_{pv} and K_{iv} are the proportional and integral coefficients for the voltage PI controller.

The power flowthrough the converter is given by (15). It can be observed that the power flow mainly depends upon f_{sw}. The constraints on f_{sw} can be found with the following two conditions.

1) The lower limit of f_{sw} lies where output power is zero.
2) The upper limit of f_{sw} is constrained by the square root term. As f_{sw} is increased, the term inside the square root becomes imaginary. Hence, a solution does not exist.

Using these constraints, the limits of f_{sw} are given by the following equation:

$$f_{\text{sw,min}} = \frac{\omega_0}{4\left[\pi + \tan^{-1}\left(\frac{-I_{l0}Z_0}{V_L}\right)\right]}$$
$$f_{\text{sw,max}} = \frac{\omega_0}{4\left[\pi + \tan^{-1}\left(\frac{1}{I_{l0}V_L Z_0}\left(\frac{V_L^2}{4} - I_{l0}^2 Z_0^2\right)\right)\right]}. \quad (23)$$

These f_{sw} limits are used to set the saturation limits of the converter through the saturation block in the control scheme.

V. Experimental Results

A lab setup is established to verify the feasibility and effectiveness of the proposed balancing solution. As shown in Fig. 10, the source of the bipolar grid is mocked by two voltage sources V_{s1} and V_{s2} with the same voltage, and the load is mocked by an electronic load that is connected only between the neutral and $-$ pole. The balancing circuit is connected between the load and the sources. Although the load takes power only from the $-$ pole, with the effect of

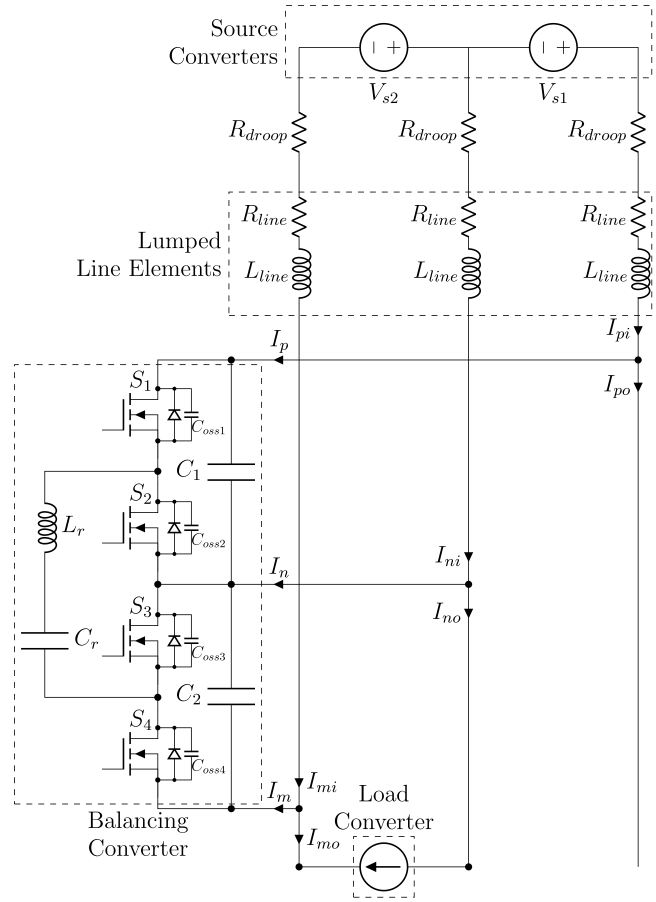

Fig. 10. Schematic of the test setup.

TABLE III
Specifications of the Laboratory Setup

Grid and converter parameters	Value
Rated power	2 kW
Grid voltage	± 350 V
Source converter voltage (V_{s1} & V_{s2})	350 V
Droop resistance (R_{droop})	15 Ω
Line resistance (R_{line})	100 $m\Omega$
Line inductance (L_{line})	34 μH
Resonant capacitance (C_r)	594 nF
DC Link capacitor (C_1 & C_2)	1 mF
SiC half-bridge module	MSCSM70AM19CT1AG
Switch output capacitance (C_{oss})	510 pF
K_{pv}	2
K_{iv}	10
L_r parameters	**Value**
Resonant inductance (L_r)	7 μH
Core material	3C90
Core area	160 mm^2
Core volume	18000 mm^3
Air gap	7.5 mm
Number of turns	14
Conductor area	6 mm^2
Number of layers	1

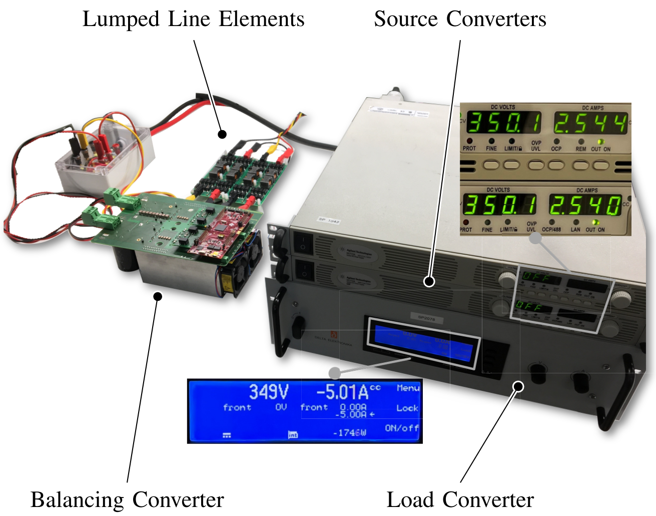

Fig. 11. Experimental setup and test result of balancing.

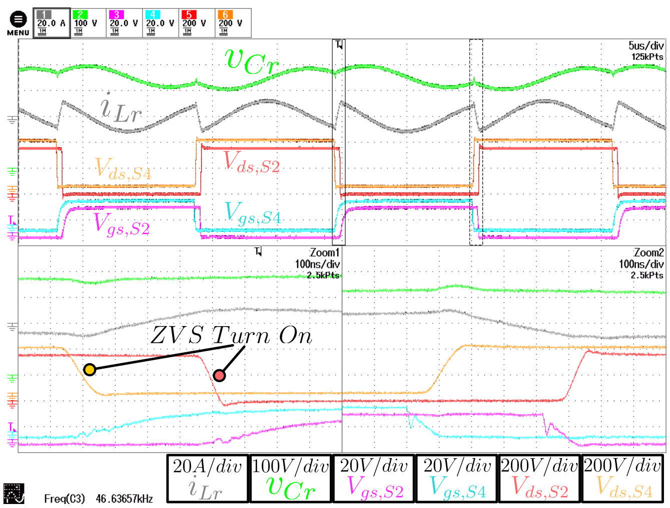

Fig. 12. Experiment results of the converter at a load current of 2.5 A. The enlarged figures at the bottom show the drain–source voltages of switches S_2 and S_4 during the transitions to confirm the soft-switching capability of the converter.

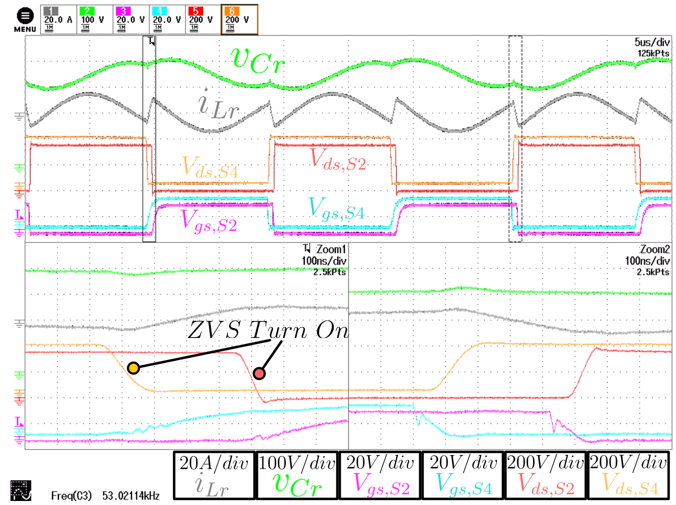

Fig. 13. Experiment results of the converter at a load current of 5 A. The enlarged figures at the bottom show the drain–source voltages of switches S_2 and S_4 during the transitions to confirm the soft-switching capability of the converter.

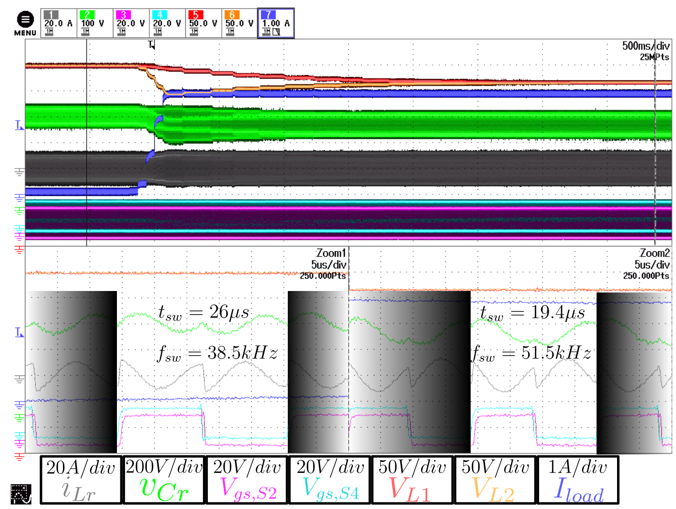

Fig. 14. Experimental results for the load current change. The left zoomed-in figure is before the load is turned on. The right zoomed-in figure is after the load is increased suddenly to 4 A.

the balancing converter, the load is evenly shared between the sources of the two poles. The experimental result demonstrating the load sharing for a load current of 5 A is shown in Fig. 11.

Figs. 12 and 13 show the switching patterns during the tests at the load currents of 2.5 and 5 A, respectively, in open-loop conditions. With the 2.5-A load current, the converter $f_{\rm sw}$ is 46.6 kHz. Similarly, with a load current of 5 A, $f_{\rm sw}$ is 53 kHz. The t_ϕ in both the tests is kept constant at 440 ns. The zoomed portions of the oscilloscope figures show the turn on (bottom left) and turn off (bottom right) of switches S_2 and S_4. These figures show that the ZVS turn on is achieved for S_2 and S_4. As the L_r current is symmetrical, it can be inferred that ZVS turn on is also achieved for S_1 and S_3.

Next, the converter is operated in a closed loop, as shown in Fig. 14. Initially, the load converter current ($I_{\rm load}$) is kept close to zero, and the control is turned on. When the control is turned on, $f_{\rm sw}$ becomes 38.5 kHz, around the converter's minimum $f_{\rm sw}$. The zoomed-in portion on the bottom left of Fig. 14 depicts this $f_{\rm sw}$. Subsequently, $I_{\rm load}$ is suddenly increased to 4 A. This increase in current leads to significant deviation in the pole voltages (V_{L1} and V_{L2}) due to the droop resistances. The control algorithm senses the difference in the poles' voltages and increases $f_{\rm sw}$. The t_ϕ is constant at 440 ns. The increase of $f_{\rm sw}$ leads to higher power flow from the upper pole to the lower pole according to (15). The pole voltages are balanced with 51.5 kHz, as shown in Fig. 14.

VI. Conclusion

In this work, a series-resonant converter for balancing a bipolar dc grid is analyzed and designed. The soft-switching capabilities of the converter with the proposed control are discussed. It is shown that the power flow depends upon

f_{sw} and ϕ between the converter's upper and lower half-bridges. However, the control relationship between f_{sw} and ϕ is decoupled with an appropriate selection of L_r. Therefore, the power control of the converter can be done only by changing f_{sw}.

The guidelines for selecting the resonant inductance and capacitance values are also discussed. The selection of the resonant inductance value depends upon the amount of power flow required and influences the converter's control characteristics (especially ϕ). For selecting resonant capacitance, costs, voltage rating, and current rating for the resonant capacitor in the operating frequency range are essential parameters that must be considered.

Finally, experimental results with different load currents at different values of f_{sw} but with a constant t_ϕ of 440 ns show that the ZVS turn on is achieved for all the switches. Furthermore. the ZVS turn-on capability of the converter using the proposed simple control method was experimentally verified.

References

[1] DC Systems B.V. (2023). *Energy Neutral Pulse Building at TU Delft DC Systems*. [Online]. Available: https://www.dc.systems/projects/pulse-building-of-delft-university-of-technology

[2] DC Systems B.V. (2023). *DC and Sustainability in the Greenhouse DC Systems*. [Online]. Available: https://www.dc.systems/projects/dc-greenhouse

[3] T. S. Hartwich, K. Sommer, T. A. Kern, and L. Haffner, "DC-Netze: Ein ganzheitlicher Systementwurf für verschiedene Schiffstypen," 2023, doi: 10.15480/882.4392.

[4] S. Yadav, Z. Qin, and P. Bauer, "Bipolar DC grids on ships: Possibilities and challenges," *E I Elektrotechnik und Informationstechnik*, vol. 139, pp. 458–467, Jun. 2022.

[5] L. Mackay, R. Guarnotta, A. Dimou, G. Morales-España, L. Ramirez-Elizondo, and P. Bauer, "Optimal power flow for unbalanced bipolar DC distribution grids," *IEEE Access*, vol. 6, pp. 5199–5207, 2018.

[6] L. Mackay, K. F. Y. Martinez, E. Vandeventer, L. Ramirez-Elizondo, and P. Bauer, "Capacitive grounding for DC distribution grids with two grounding points," in *Proc. IEEE 2nd Int. Conf. DC Microgrids (ICDCM)*, Jun. 2017, pp. 76–80.

[7] L. Mackay, E. Vandeventer, and L. Ramirez-Elizondo, "Circulating net currents in meshed DC distribution grids: A challenge for residual ground fault protection," *IEEE Trans. Power Del.*, vol. 33, no. 2, pp. 1018–1019, Apr. 2018.

[8] S. Rivera, R. Lizana F., S. Kouro, T. Dragicevic, and B. Wu, "Bipolar DC power conversion: State-of-the-art and emerging technologies," *IEEE J. Emerg. Sel. Topics Power Electron.*, vol. 9, no. 2, pp. 1192–1204, Apr. 2021.

[9] Y. Zhao, W. Huang, and F. Bu, "DC voltage balancing strategy of a bipolar-output active rectifier for more electric aircraft based on zero vector redistribution," *IEEE Access*, vol. 9, pp. 139657–139667, 2021.

[10] V. F. Pires, A. Cordeiro, D. Foito, and J. F. Silva, "A DC–DC converter with capability to support the voltage balance of DC bipolar microgrids," in *Proc. 11th Int. Conf. Renew. Energy Res. Appl. (ICRERA)*, Sep. 2022, pp. 50–55.

[11] J. Lago, J. Moia, and M. L. Heldwein, "Evaluation of power converters to implement bipolar DC active distribution networks—DC–DC converters," in *Proc. IEEE Energy Convers. Congr. Expo.*, Sep. 2011, pp. 985–990.

[12] J. Moia, J. Lago, A. J. Perin, and M. L. Heldwein, "Comparison of three-phase PWM rectifiers to interface AC grids and bipolar DC active distribution networks," in *Proc. 3rd IEEE Int. Symp. Power Electron. Distrib. Gener. Syst. (PEDG)*, Jun. 2012, pp. 221–228.

[13] G. Van den Broeck, S. De Breucker, J. Beerten, J. Zwysen, M. Dalla Vecchia, and J. Driesen, "Analysis of three-level converters with voltage balancing capability in bipolar DC distribution networks," in *Proc. IEEE 2nd Int. Conf. DC Microgrids (ICDCM)*, Germany, Jun. 2017, pp. 248–255.

[14] F. Wang, Z. Lei, X. Xu, and X. Shu, "Topology deduction and analysis of voltage balancers for DC microgrid," *IEEE J. Emerg. Sel. Topics Power Electron.*, vol. 5, no. 2, pp. 672–680, Jun. 2017.

[15] G. Van den Broeck, J. Beerten, M. D. Vecchia, S. Ravyts, and J. Driesen, "Operation of the full-bridge three-level DC–DC converter in unbalanced bipolar DC microgrids," *IET Power Electron.*, vol. 12, no. 9, pp. 2256–2265, Aug. 2019.

[16] P. Najafi, A. H. Viki, and M. Shahparasti, "Evaluation of feasible interlinking converters in a bipolar hybrid microgrid," *J. Modern Power Syst. Clean Energy*, vol. 8, no. 2, pp. 305–314, Mar. 2020.

[17] K. Sano and H. Fujita, "Voltage-balancing circuit based on a resonant switched-capacitor converter for multilevel inverters," *IEEE Trans. Ind. Appl.*, vol. 44, no. 6, pp. 1768–1776, Nov. 2008.

[18] K. Sano and H. Fujita, "Performance of a high-efficiency switched-capacitor-based resonant converter with phase-shift control," *IEEE Trans. Power Electron.*, vol. 26, no. 2, pp. 344–354, Feb. 2011.

[19] W. Hang, Z. Xiang-Jun, Z. Mei-Mei, H. Ying-Ying, Z. Xiao, and Y. Xu, "5L full-scale converter with a DC-link flying-capacitor auxiliary bridge leg for large direct-drive wind turbines," *IET Electr. Power Appl.*, vol. 11, no. 6, pp. 1001–1012, Jul. 2017.

[20] Y. Lei, Y. Zhuang, F. Liu, X. Diao, and Y. Huang, "A general four-port converter with series LC voltage balancer for bipolar DC microgrid," *IEEE Trans. Ind. Electron.*, vol. 70, no. 12, p. 12311, Dec. 2023.

[21] A. Cervera, M. Evzelman, M. M. Peretz, and S. Ben-Yaakov, "A high-efficiency resonant switched capacitor converter with continuous conversion ratio," *IEEE Trans. Power Electron.*, vol. 30, no. 3, pp. 1373–1382, Mar. 2015.

[22] H. Zhu, J.-S. Lai, A. R. Hefner, Y. Tang, and C. Chen, "Modeling-based examination of conducted EMI emissions from hard- and soft-switching PWM inverters," *IEEE Trans. Ind. Appl.*, vol. 37, no. 5, pp. 1383–1393, Sep. 2001.

[23] S. Yadav, Z. Qin, and P. Bauer, "Cases of soft switching in a series resonant balancing converter for bipolar DC grids," in *Proc. IECON 48th Annu. Conf. IEEE Ind. Electron. Soc.*, Oct. 2022, pp. 1–6.

[24] M-J. Pan and C. A. Randall, "A brief introduction to ceramic capacitors," *IEEE Elect. Insul. Mag.*, vol. 26, no. 3, pp. 44–50, May 2010.

[25] X. Xu et al., "Advances in class-I C0G MLCC and SMD film capacitors," in *Proc. 28th Symp. Passive Compon. (CARTS USA)*, Newport Beach, CA, USA, 2008, pp. 449–461.

[26] J. Bultitude, L. Jones, B. Xu, J. Magee, and R. Phillips, "An evaluation of BME C0G multilayer ceramic capacitors as building blocks for DC-link capacitors in 3-D power electronics," in *Proc. Int. Symp. 3D Power Electron. Integr. Manuf. (3D-PEIM)*, Jun. 2016, pp. 1–18.

[27] A. Gurav, X. Xu, J. Magee, R. Phillips, and T. Ashburn, "Advances in ceramic capacitors for high temperature applications," in *Proc. Additional Conf. (Device Packag., HiTEC, HiTEN, CICMT)*, Jan. 2015, pp. 134–141.

[28] S. Menzel, *ABC of Capacitors: Basics, Characteristics and Capacitor*, vol. 15. Niedernhall, Germany: Würth Electronik, 2015.

[29] V. F. Pires, A. Cordeiro, C. Roncero-Clemente, S. Rivera, and T. Dragicevic, "DC–DC converters for bipolar microgrid voltage balancing: A comprehensive review of architectures and topologies," *IEEE J. Emerg. Sel. Topics Power Electron.*, vol. 11, no. 1, pp. 981–998, Feb. 2023.

[30] Y. Zhang, C. Chen, T. Liu, K. Xu, Y. Kang, and H. Peng, "A high efficiency model-based adaptive dead-time control method for GaN HEMTs considering nonlinear junction capacitors in triangular current mode operation," *IEEE J. Emerg. Sel. Topics Power Electron.*, vol. 8, no. 1, pp. 124–140, Mar. 2020.

[31] R. W. Erickson and D. Maksimović, *Fundamentals of Power Electronics*. Cham, Switzerland: Springer, 2020.

[32] B. T. Lynch, "Under the hood of a DC/DC boost converter," in *TI Power Supply Design Seminar*, vol. 2009. Dallas, TX, USA: Texas Instruments Inc., 2008, p. 26.

[33] G. Yu, S. Yadav, J. Dong, and P. Bauer, "Revisiting the reverse switched current of buck, boost and buck-boost converters in voltage-mode TCM-ZVS control considering parasitic resistances," *IEEE Trans. Power Electron.*, early access, 2024, doi: 10.1109/TPEL.2024.3382051.